



Effect of Ni/Mn Ordering on Elementary Polarizations of $\text{LiNi}_{0.5}\text{Mn}_{1.5}\text{O}_4$ Spinel and Its Nanostructured Electrode

Hyung-Man Cho^{a,b,*} and Ying Shirley Meng^{a,b,**,z}

^aDepartment of NanoEngineering, University of California San Diego, La Jolla, California 92093, USA

^bMaterials Science and Engineering, University of California San Diego, 9500 Gilman Drive, La Jolla, California 92093, USA

Elementary polarizations of $\text{LiNi}_{0.5}\text{Mn}_{1.5}\text{O}_4$ spinel materials with disordered structure (space group, $Fd\bar{3}m$) and ordered structure (space group, $P4_332$) are quantitatively analyzed in order to clarify how the differences in crystallographic structure affect the rate performance of the cathode materials. A comparative analysis of the disordered and ordered structures disclosed that the nickel and manganese ordering in the spinel-framework would distinctly aggravate the charge-transfer reactions. Furthermore, the ordinary approach to increase the rate performance of an electrode through a reduction of the diffusion lengths and an enlargement of the active surface area with the nano-structured electrode which consists of the disordered spinel revealed that both charge-transfer and solid-state diffusion resistances reduced, but the resistance of lithium migration through the surface films increased significantly. © 2013 The Electrochemical Society. [DOI: 10.1149/2.059309jes] All rights reserved.

Manuscript submitted January 8, 2013; revised manuscript received June 20, 2013. Published July 10, 2013. This was Paper 3530 presented at the Honolulu, Hawaii, Meeting of the Society, October 7–12, 2012.

The recognition of the world-wide energy crisis boosted the development of environmentally benign energy infrastructures, where energy storage is one of the key components. Among the various energy storage systems, lithium-ion batteries have been considered as the best candidate for maximizing energy efficiency. However, state-of-the-art battery technology is still insufficient to meet the requirements for high-power applications, for instance, electric vehicles.^{1,2} $\text{LiNi}_{0.5}\text{Mn}_{1.5}\text{O}_4$ spinel materials have attracted particular attention as a promising candidate for replacing the current commercially available positive materials, e.g. LiCoO_2 , of lithium-ion batteries.^{3–5} Spinel $\text{LiNi}_{0.5}\text{Mn}_{1.5}\text{O}_4$ provides a high-voltage plateau at ~ 4.7 V (vs. Li/Li^+) and thus enables relatively higher energy density (theoretical specific capacity, 146.72 mA h g^{-1}). Inherently, the spinel-framework structure makes the lithium ion transportation inside the bulk materials (solid-state diffusion) easier because the spinel structure is based on a three-dimensional MO_2 (M: transition metals) host and the vacancies in transition metal layer along [111] cubic structure ensure three-dimensional lithium pathways. In the structure of LiM_2O_4 spinel, M cations occupy the octahedral site but $\frac{1}{4}$ of them are located in the lithium layer along [111]_{cubic}, leaving $\frac{1}{4}$ of the sites in transition metal layer vacant. Lithium ions occupy the tetrahedral sites in lithium layer that share faces with these empty octahedral sites in the transition metal layer.⁶

Many researchers have endeavored to study the two different crystallographic structures of $\text{LiNi}_{0.5}\text{Mn}_{1.5}\text{O}_4$ spinel material: the disordered structure with the space group $Fd\bar{3}m$ and the ordered structure with the space group $P4_332$.^{4,7–9} Despite its importance to the overall performance, there is still a lack of understanding of how ordering of nickel and manganese on the octahedral sites affects the elementary reactions steps involved in their electrochemical operation. In this work, we have used a combination of electrochemical impedance spectroscopy and the theoretical analysis of their equivalent circuits,^{10–12} to quantitatively analyze and compare the proportional contribution of the elementary reaction steps to the total polarization of the disordered and ordered structures. Furthermore, the nano-structured electrode is prepared in order to improve its rate performance, and the variation of its elementary reaction steps are analyzed and compared to those in the conventional composite electrodes. Since the instantaneous power density is one of the key performance factors for designing the battery for transportation application, we focus on the analysis of the elementary reaction steps at the charged state of the battery at the initial discharging time. This work serves as a good starting point to funda-

mentally understand the nano-structured electrode kinetics, with the goal of designing batteries possessing the ideal performance.

Experimental

Powder materials preparation and composite electrode fabrication.— $\text{LiNi}_{0.5}\text{Mn}_{1.5}\text{O}_4$ spinel materials were synthesized using a previously reported sol-gel method.⁵ The resulting gel precursors were decomposed at 500°C for 12 hours in air and then calcinated at 900°C for 14 hours in air. The as-prepared disordered structure powders were made to the ordered structure by annealing at 700°C for 48 hours in air.

For the composite electrode fabrication, the slurry consisting of 80 wt% active materials, 10 wt% acetylene carbon black, and 10 wt% poly(vinylidene fluoride) (PVdF) in N-methyl pyrrolidone (NMP) were pasted on the aluminum foil current collector, dried overnight in a vacuum oven at 80°C , and punched and pressed uniaxially. In order to minimize the effect of the porosity, the similar loading weights of the cathode electrodes are employed in this work (0.01378 g and 0.01384 g for the disordered and ordered structures, respectively).

Nano-structured electrode fabrication.— $\text{LiNi}_{0.5}\text{Mn}_{1.5}\text{O}_4$ spinel materials were also prepared as a nano-fiber/nano-wire structure via a sol-gel based template-assisted synthesis method. Commercially available polycarbonate porous membrane (Whatman, P/N: 7060-2502) of 200 nm ($= 0.2$ μm) pore diameter as a template was immersed into a precursor sol. Fully soaked templates were placed on a platinum foil current collector, and gelation was carried out in the drying oven. The oxygen plasma etching system (Trion RIE/ICP dry etcher) was used to remove the template. Eventually, as-prepared protruding nano-structured electrode was crystallized with 900°C heat-treatment for only 2 hours. The active weight of the nano-structured electrode is estimated from the calculated volume and the observed porosity, the value is in good agreement with the measured value by an electronic balance with 0.1 mg accuracy.

Materials characterization.— The morphologies and size distributions were examined with a scanning electron microscope (SEM, Phillips, XL30) and a transmission electron microscope (TEM, FEI Tecnai G2 Sphera cryo-electron microscope). For the TEM, the nano-structured fibers were suspended on a 300 mesh copper grid with lacey carbon. In order to identify the crystalline phase of the synthesized materials, powder X-ray diffraction (XRD, Bruker D8) measurements using $\text{Cu K}\alpha$ radiation were employed. XRD data were obtained for the range $2\theta = 10\text{--}80^\circ$, with a scan rate of $0.02^\circ \text{ s}^{-1}$. XRD data analysis was carried out by the Rietveld refinement using the FullProf software package. The molar ratio of Ni and Mn of the samples were

*Electrochemical Society Student Member.

**Electrochemical Society Active Member.

^zE-mail: shirleymeng@ucsd.edu

analyzed by inductive coupled plasma optical emission spectroscopy (ICP-OES Perkin-Elmer Plasma 3700).

Electrochemical characterization.— The methodology to analyze quantitatively the effect of the elementary impedances on the total dc polarization was introduced in the previous work.^{10–12} In this work, with the use of such methodology, the effect of the crystalline structure difference (disordered and ordered structures) was compared. In addition, the effects of nano-structured electrode on the rate performance were investigated. For the electrochemical experiments, the custom-made three-electrode cell configuration^{10–13} was employed. The prepared electrodes and lithium metal were used for the positive and negative electrodes, respectively. For the reference electrode, the copper wire was placed in between separators (Celgard C480). Before the tests, elemental lithium was cathodically coated on the bare copper wire by taking lithium metal electrode as a counter electrode. The electrolyte was a 1 M solution of lithium hexafluorophosphate (LiPF₆) in a 1:1 volume mixture of ethylene carbonate (EC) and dimethyl carbonate (DMC). All the cells used for the electrochemical tests was assembled in a glove box (MBraun, Germany) filled with purified argon gas (H₂O level of <1 ppm).

The as-prepared cell was charged and discharged three times between 3.5 and 4.85 V (vs. Li/Li⁺) at a rate of 0.1 C (= C/10) (the theoretical specific capacity of 146.72 mAh g⁻¹ of LiNi_{0.5}Mn_{1.5}O₄ was assumed to convert the current density into C rate). The electrochemical impedance measurement was carried out in the frequency range of 100 kHz to 10 mHz at a cell potential of 4.85 V (vs. Li/Li⁺) using a signal with an amplitude of 10 mV. Pulse discharge tests were performed right after the impedance test. For the pulse discharge test, a variety of pulse discharge currents were applied when a constant potential of 4.85 V (vs. Li/Li⁺) was obtained at the open circuit. In order to get the open circuit voltage with negligible lithium contents, all the cells was charged with the application of the low constant current rate, C/20, and the constant voltage was applied subsequently until it has an equilibrated potential after an extended rest at open circuit. We chose low lithium content (high voltage) because it is well known that the electrode/electrolyte interface is less stable at the high voltage where surface film is formed.¹⁴ A Solartron 1287 electrochemical interface was employed to carry out all of the galvanostatic/potentiostatic tests. For the electrochemical impedance measurements, the Solartron 1287 electrochemical interface was coupled with a Solartron 1455A frequency response analyser.

Results and Discussion

Characterizations of Powder materials and nano-structured electrodes.— Typical morphologies of the LiNi_{0.5}Mn_{1.5}O₄ spinel materials with disordered and ordered structures are shown in the SEM images of Figure 1a and 1b. When disordered structure powders calcinated at 900°C, the primary particles formed polygonal morphology with the dust-like small particles at the surface as shown in Figure 1a. The average particle size was about 700 nm (in the range of 400–1000 nm). After further annealing at 700°C, as-prepared ordered structure powders (Figure 1b) also had polygonal morphology and similar particle size, about 700 nm (in the range of 400–1000 nm). It is notable that the tiny particles at the surface of the disordered structure disappeared completely with the transformation from the disordered structure to ordered structure. It has been reported that the separate small particles are the rock-salt phase that is commonly observed in the synthesis of LiNi_{0.5}Mn_{1.5}O₄ spinel materials, especially over 700°C calcination temperatures.^{7–9}

For the nano-structured electrode of LiNi_{0.5}Mn_{1.5}O₄ spinel materials, sol-gel based template synthesis method^{15–17} was employed in this work, as described in the experimental section. Figure 1c shows the SEM image of as-prepared nano-structured electrode, depicting the nano-fibers protruding from the surface of the platinum current collector, like shrubs with twisted branches. The average diameter of the nano-fibers and length were approximately 160 nm and 12 μm, respectively. A closer look at the nano-structured electrodes with the

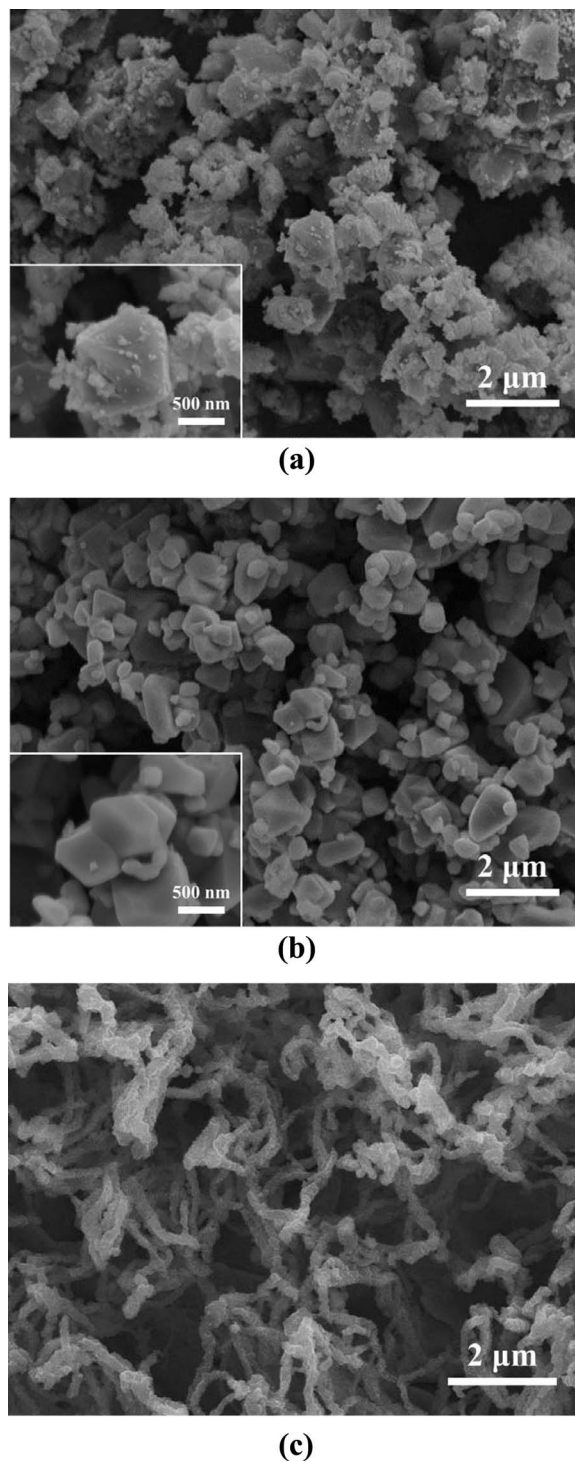
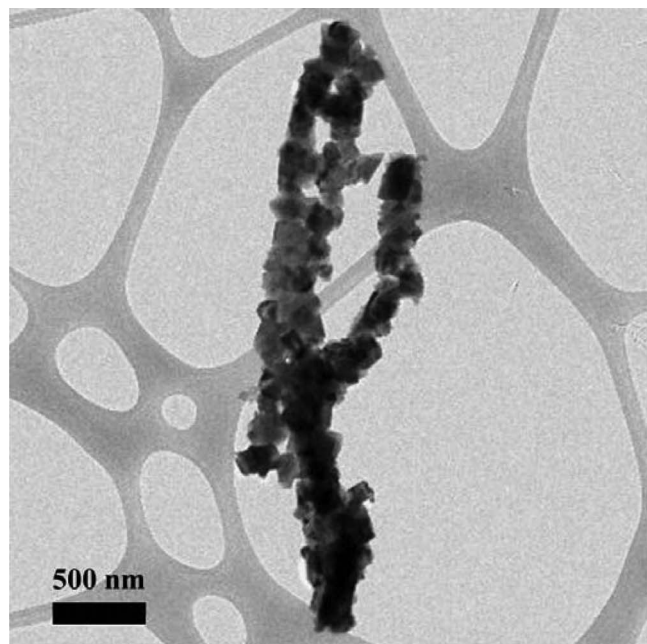


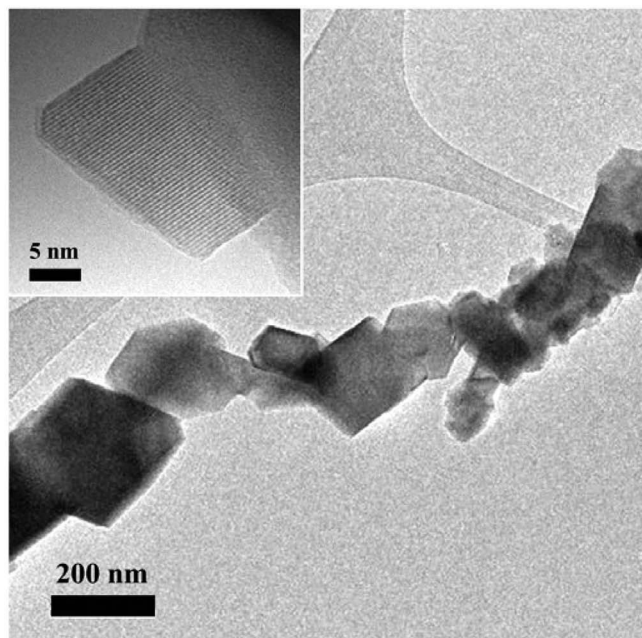
Figure 1. Scanning electron micrographs of LiNi_{0.5}Mn_{1.5}O₄ (a) disordered structure and (b) ordered structure powders synthesized via a sol-gel method, and (c) top views of nanowire prepared via sol-gel based template synthesis method.

TEM images in Figure 2 reveals that it is constructed with a series of connected particles (ca. 160 nm of the average particle size in the range of 50–200 nm).

In order to identify the structural properties of the materials, the XRD patterns are collected and compared as shown in Figure 3. The nominal LiNi_{0.5}Mn_{1.5}O₄ spinel material is cubic close packed with lithium on the tetrahedral sites. The disordered structure with nickel and manganese disordering on the octahedral sites has the



(a)



(b)

Figure 2. Transmission electron micrographs of (a) and (b) nanowire prepared via sol-gel based template synthesis method.

space group, $Fd\bar{3}m$, while, the ordered structure has the space group, $P4_332$.^{18,19} The Rietveld refinement patterns of the XRD for both disordered and ordered structures indicated an excellent agreement with those reported previously in the literatures.^{9,19,20} In the case of the disordered structure (Figure 3b), small peaks were observed at $2\theta = 37.6^\circ$, 43.7° , and 63.5° , indicative of a cation-rich rock salt phase (as mention in the Figure 1a). Recently, it is reported that this rock salt phase contains both manganese and nickel in a lower ratio than in the spinel phase.⁷ The superstructure peaks of the ordered structure (Figure 3c) were confirmed with the small peaks observed at

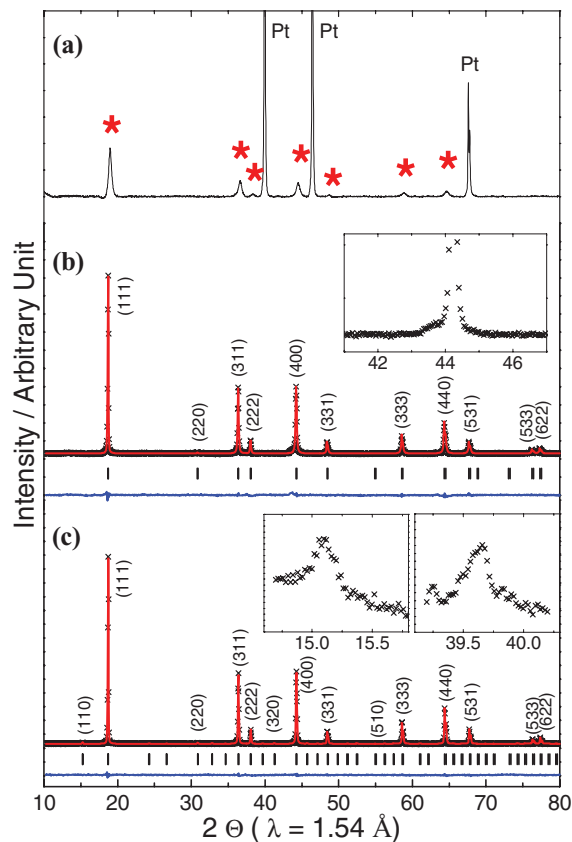


Figure 3. XRD patterns of (a) as-prepared nanowire electrode. The Rietveld refinement results from XRD patterns collected from $\text{LiNi}_{0.5}\text{Mn}_{1.5}\text{O}_4$ (b) disordered structure and (c) ordered structure powders synthesized via a sol-gel method. The black crosses represent the observed pattern, the red line corresponds to the calculated diffraction pattern and the blue is the difference pattern.

$2\theta = 15.3^\circ$, and 39.7° , consistent with the literature report.¹⁹ The lattice parameter of the disordered structure, 8.1739 \AA , is larger than that of the ordered structure, 8.1653 \AA . The presence of Mn^{3+} in the spinel phase, which can be derived from the 4 V (vs. Li/Li^+) plateau shoulder in charge/discharge curves, results in a larger lattice parameter.^{8,21} The XRD patterns of the nano-structured electrode discloses that the nano-structured electrode consists of the $\text{LiNi}_{0.5}\text{Mn}_{1.5}\text{O}_4$ spinel materials, as shown in Figure 3a. Since the peaks of the nano-structured electrode are relatively weak and broad, attempts to account for them by introducing the phase into the Rietveld refinements did not yield satisfactory results. Nevertheless, all the peak positions are well-matched with the powder materials synthesized via a sol-gel method, except the peaks from the platinum current collector (see asterisks in Figure 3a).

The Ni and Mn molar ratio of the pristine materials were checked by ICP-OES analysis (Table I). Although a cation-rich rock salt phase

Table I. Ni:Mn molar ratio of the pristine $\text{LiNi}_{0.5}\text{Mn}_{1.5}\text{O}_4$ materials, disordered structure ($Fd\bar{3}m$), ordered structure ($P4_332$), and nano-wires as measured by ICP-OES.

Sample	Ni:Mn ratio	
	experimental (ICP-OES)	Theoretical
Disorder ($Fd\bar{3}m$)	3.02	
Order ($P4_332$)	3.05	3.00
Nano-wires	3.01	

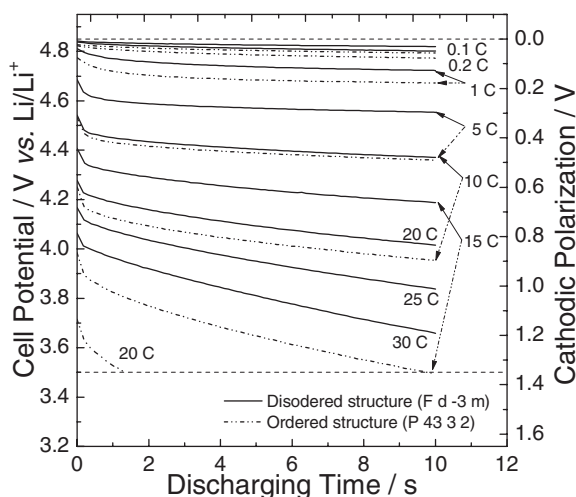


Figure 4. Experimental cell potential (or cathodic polarization) transients during the cathodic pulse discharging for 10 s at different discharging rates obtained from $\text{LiNi}_{0.5}\text{Mn}_{1.5}\text{O}_4$ disordered and ordered structure.

appeared in the disordered structure, the molar ratio of Ni and Mn is in good agreement with the theoretical ratio in all samples.

Effect of the crystalline structures on the elementary electrode reactions.— Figure 4 presents the cell potential (or cathodic polarization) transients of the as-prepared disordered and ordered structures during constant current discharging for 10 seconds at different discharging rates. Right after the pulse discharging, the transients showed a rapid drop and a relatively slow decrease in potential with time. The transients of the disordered structure (solid lines) fell slower than those of the ordered structure (dotted lines). The maximum discharging rate of the disordered structure was 30 C; the cell potential still remained above the low cutoff voltage of 3.5 V (vs. Li/Li^+) throughout the whole discharging time. However, at the discharging rate of 15 C, the cell potential transient of the ordered structure reached the cutoff voltage before 10 seconds. This means that the disordered structure enables a more prolonged operation at high current drains compared to the ordered structure; i.e., the disordered structure shows better rate performance than the ordered structure, which is consistent with earlier reports.^{4,7,8,18–20}

To explore how a dissimilarity of nickel and manganese ordering in the crystal structure affects the elementary reaction steps and their contribution to the total dc polarization, the differentiation of the resistive elements was done by using the electrochemical impedance spectroscopy, as shown in Figure 5. For the positive electrodes (intercalation process, Figure 5), it is generally agreed that the depressed semicircle in the high-frequency range reflects lithium-ion migration through multilayer surface films, and, in the medium-frequency range, nearly perfect (undeformed) semicircle is attributed to charge-transfer resistance coupled with the double layer capacitance at the interface between the surface film and intercalation materials. Also, the inclined line in the low-frequency range is responsible for the solid-state lithium diffusion through the intercalation materials, known as the Warburg impedance.^{22–26} On the other hand, the origin and mechanism of lithium negative electrode reactions are not clear at this point. The detailed analysis of the lithium negative electrode is beyond the scope of this work.

To quantitatively analyze the obtained impedance spectra, the mechanism-based equivalent circuits which model the elementary reactions was adopted, as shown in the insets of Figure 5. First resistance, R_Ω , indicates the uncompensated ohmic resistance. A series of the resistance and constant phase element (CPE), R_{f1} - CPE_{f1} and R_{f2} - CPE_{f2} , represents the lithium migration through multilayer surface films, which can be simplified into porous part and compact interphase. From the reported literatures,^{24,26–29} it is demonstrated that

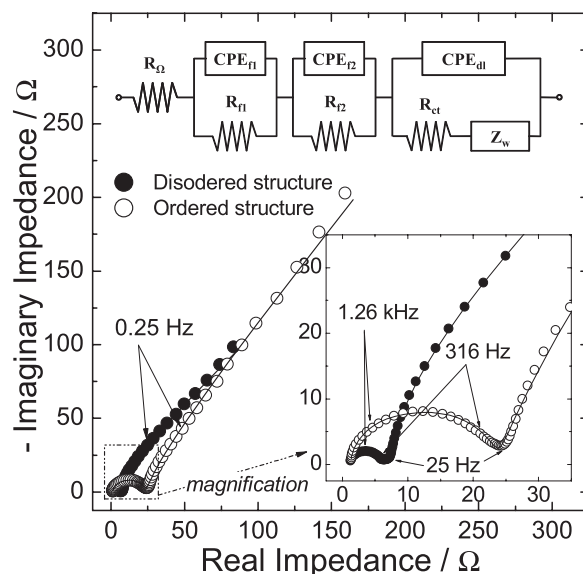


Figure 5. Impedance spectra of (a) the positive and (b) negative electrodes, obtained at a cell potential of 4.85 V (vs. Li/Li^+). The insets on (a) and (b) are the equivalent circuits to model the reactions in the working and counter electrodes, respectively. Solid lines were determined from the CNLS fittings of the impedance spectra to the equivalent circuits.

Li intercalation processes of Li_xMO_y materials, such as $\text{Li}_x\text{Mn}_2\text{O}_4$, Li_xNiO_2 , and Li_xCoO_2 , show similarity with the graphite materials, and thus, typical impedance spectra of Li_xMO_y materials are also similar with that of the graphite materials. Therefore, those impedance spectra were nicely fitted with the multilayer surface film model. In this work, the impedance spectra of $\text{LiNi}_{0.5}\text{Mn}_{1.5}\text{O}_4$ spinel are also analogous to other intercalation materials, which contain a high frequency semicircle which is basically potential invariant. This similarity justifies the adoption of the impedance model with the multilayer surface films. And a pair of the resistance and CPE, R_{ct} - CPE_{dl} , shows the charge-transfer resistance and double layer capacitance. In addition, the Warburg impedance, Z_w , indicates the solid-state diffusion. All the electrical parameters in the equivalent circuit were determined from the CNLS (complex non-linear least squares) fitting method, and are summarized in the Table II. The equivalent circuit based on the obtained electrical parameters was re-constructed toward the circuit simulation, as explained in the previous literatures.^{10,11}

Using the circuit simulation, the variations in the total elementary polarizations of the disordered and ordered structures were obtained with the discharging time at a discharging rate of 5 C, and then, its time-dependent contributions of the elementary resistances to the total polarization were obtained as shown in Figure 6a and 6b. The charge-transfer reaction and solid-state diffusion reaction are the first and second largest contributions of the total dc polarization for both the disordered and ordered structures. It also proved that the contribution of lithium migration through the surface films is relatively trivial. In addition, it is noteworthy that the contribution of the charge-transfer resistance of the ordered structure shows over 50% at 10 s discharging, which is considerably higher than that of the disordered structure.

Elementary reaction behaviors of the nano-structured electrode.— The above results demonstrated that the charge-transfer and diffusion reactions are the two major sources responsible for the power density. Especially, it showed that the nickel and manganese ordering in the spinel structure aggravated the charge-transfer reactions. Now, it would be interesting to see what happens to the nano-structured electrode. The nano-structured electrode has been considered as a promising way to achieve utmost power density without much sacrifice of energy density. Its short diffusion lengths and relatively large surface area will reduce the resistance to interfacial reactions and thus

Table II. Electrical parameters of the working electrodes, determined from the complex non-linear least squares (CNLS) fitting of impedance spectra to the equivalent circuit. This also includes the diffusion coefficient, diffusion length and some calculated values.

	CPE _{f1} ¹				CPE _{f2} ¹				CPE _{dl} ¹				A_{ω} ² $\Omega \text{ s}^{-0.5}$	D ³ $\times 10^{-12} \text{ m}^2 \text{ s}^{-1}$	L ⁴ nm	R_D ⁵ Ω	C_D ⁵ mF	r ⁵ $\times 10^6 \Omega \text{ m}^{-1}$	c ⁵ $\times 10^6 \text{ F m}^{-1}$
	R_{Ω} Ω	R_{f1} Ω	C $\mu\text{F s}^{\eta-1}$	η	R_{f2} Ω	C $\mu\text{F s}^{\eta-1}$	η	R_{ct} Ω	C mF $\text{s}^{\eta-1}$	η									
Disorder ($d = 3 \text{ m}$)	1.01	4.86	12.01	0.88	1.65	4103	0.73	18.73	6.26	0.99	51.14	7.76	700	12.85	4.91	18.36	0.007		
Order (P 4 ₃ 3 2)	1.19	6.67	3.41	1	15.85	27.06	0.85	99.27	5.56	0.79	87.57	1.91	700	44.32	5.78	63.31	0.008		
Nano-wires	3.05	18.8	71.44	0.92	78.62	104.6	0.90	12.44	7.88	1	10.55	14.7	160	0.44	3.95	2.75	0.025		

¹Constant phase element (CPE) was expressed in the form of $C(j\omega)^{\eta}$ ($0.5 < \eta < 1$).

² A_{ω} is the Warburg coefficient.

³ D at 4.85 V (vs. Li/Li⁺) was estimated from the GITT.^{38,39}

⁴ L was roughly estimated to be the radius of particle from the SEM and TEM observation.

⁵ $R_D = A_{\omega} \cdot L \cdot D^{-0.5}$, $C_D = L^2 \cdot R_D^{-1} \cdot D^{-1}$, $r = R_D \cdot L^{-1}$, $c = C_D \cdot L^{-1}$.

accelerate electrode kinetics.^{30–33} In this work, the nano-structured electrode was prepared via the sol-gel based template synthesis,^{15–17} as shown in Figure 1c. The conventional composite electrodes consisting of nano-size materials, such as nano-particles, and nano-rods, might be insufficient due to the inherent imperfection of the structure.

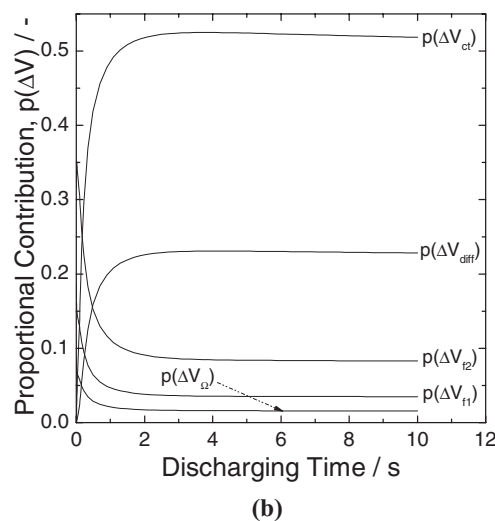
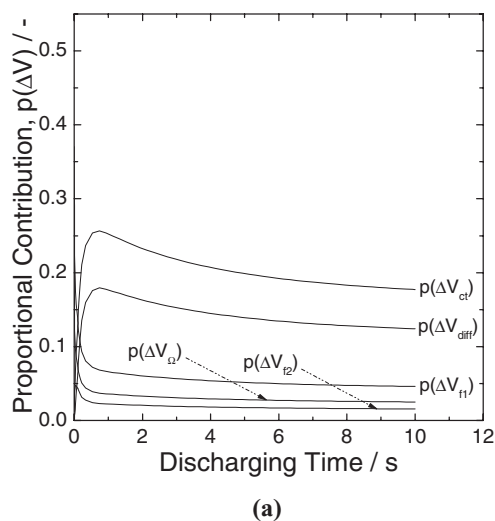


Figure 6. Time-dependent proportional contribution of elementary impedances to total polarization at a discharging rate of 5C for LiNi_{0.5}Mn_{1.5}O₄ (a) disordered structure and (b) ordered structure.

When the active species around the nano-particles become exhausted, the overall electrode reactions deteriorate rapidly by the transport of the species toward the porous structure. However, the one-dimensional nano-structured electrodes, which stand up from the current collector, not only secure the straight path for the facile movement of the active species in the electrolyte, but also provide continuous pathways for electron transport.

The cell potential (or cathodic polarization) transients of the as-prepared nano-structured electrode during the 10 s current pulse at a variety of discharging rates are shown in the Figure 7. All the transients show an abrupt drop at the moment of the application of the current, followed by a gentle decrease in potential with time. It is noted that even at the very high discharging rate of 30 C, its cathodic polarization, 0.5 V, was less than half of the maximum polarization, 1.35 V. There is no doubt that the nano-structured electrode improved the power density significantly. The differentiation of the resistive elements was further investigated in the same manner as described above.

Figure 8 shows the impedance spectra of the nano-structured LiNi_{0.5}Mn_{1.5}O₄ spinel materials obtained after three charge and discharge cycles. Using the same equivalent circuit model, all the electrical parameters were estimated by the CNLS fitting method (Table II). When comparing between the nano-structured electrode and the previous powder composite electrodes, the real impedances of lithium migration from internal compact interphase, R_{f2} , and charge-transfer reaction, R_{ct} , and Warburg coefficient, A_{ω} , are summarized in Figure 9.

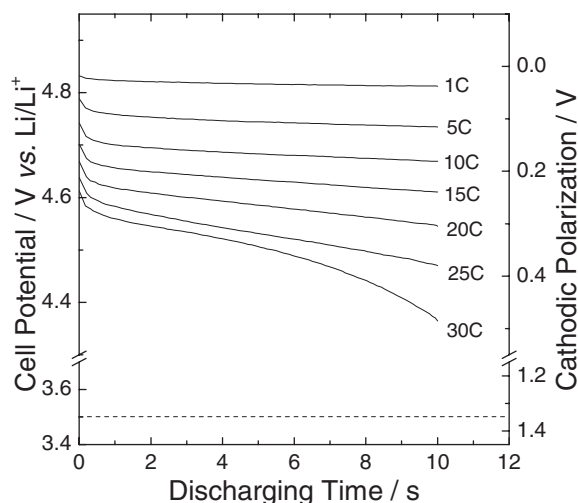


Figure 7. Experimental cell potential (or cathodic polarization) transients during the cathodic pulse discharging for 10 s at different discharging rates obtained from nanowire prepared via sol-gel based template synthesis method.

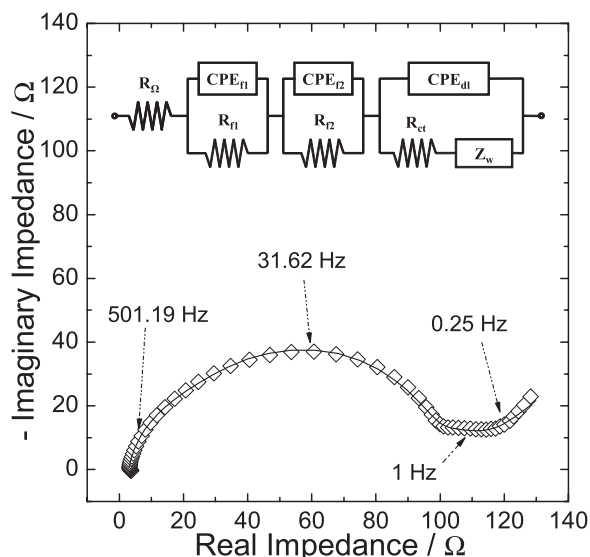


Figure 8. Impedance spectra of the nanowire prepared via sol-gel based template synthesis method. The insets are the equivalent circuits to model the working electrode reaction. Solid lines were determined from the CNLS fittings of the impedance spectra to the equivalent circuits.

A closer look at the changes in the resistances measured in the composite electrodes and nano-structured electrode shows that the resistance R_{ct} from the charge-transfer reaction and the Warburg coefficient A_w reduced. In the case of the charge-transfer reaction, the resistance of the nano-structured electrode was ca. 1.5 times smaller than that of the disordered structure composite electrode. In addition, the Warburg coefficient of the nano-structured electrode was ca. 4.8 times lower compared to the disordered structure composite electrode. This indicates that the strategy employed to reduce the impedances with the reduced diffusion length and the increased active surface area is successful.

However, it is also noteworthy that the resistance from the lithium migration through the multilayer surface films increased significantly. Especially, the resistance of the inner compact interphase, R_2 , became the largest elementary impedance. It is increased by ca. 5.0 times compared to that of the ordered structure. The most probable reason for this increase of the surface film resistances is the oxidation of the electrolyte. It is well-known that the high voltage operation of the $\text{LiNi}_{0.5}\text{Mn}_{1.5}\text{O}_4$ spinel materials over 4.3 V (vs. Li/Li^+) oxidizes

the liquid-carbonate electrolyte.³⁴ This detrimental reaction occurs during cycling, and thus leads to increasing the passivation layers on the surface. The increased surface area of the nano-structured electrode aggravates this undesirable process.^{7,35}

Notwithstanding the deteriorated surface film resistance, the origin of the improved rate performance (or power density) in the nano-structured electrode (Figure 7) is still reasonably explained with the reduced the charge-transfer and diffusion resistances. The highest frequencies of the arc from the charge-transfer reaction and the inclined line for the diffusion reaction were estimated to be 2.5 Hz and 0.25 Hz, respectively (Figure 8). This implies that the charge-transfer reaction starts to dominate the discharging transient only after 0.4 seconds; and, the diffusion reaction after 4 seconds. However, for the further enhancement of the nano-structured $\text{LiNi}_{0.5}\text{Mn}_{1.5}\text{O}_4$ spinel materials as battery electrodes, it is quite clear that the surface modifications, which stabilize the interface between the electrode and electrolyte, should be followed. The nano-structured electrode shows strong evidence of Mn^{3+} ions at the surface of $\text{LiNi}_{0.5}\text{Mn}_{1.5}\text{O}_4$, which can lead to Mn^{2+} dissolving into the electrolyte and migrating to the anode.^{4,8,36,37} The long term cycling of the nano-structured $\text{LiNi}_{0.5}\text{Mn}_{1.5}\text{O}_4$ spinel and its surface characteristics will be discussed in a separate paper.

Conclusions

In this work, dependence of the contribution of elementary impedances to total dc polarization on battery discharging process was successfully analyzed with two different structures of the $\text{LiNi}_{0.5}\text{Mn}_{1.5}\text{O}_4$ spinel materials, disordered (space group, $Fd\bar{3}m$) and ordered (space group, $P4_332$) structures, from a combination of electrochemical impedance spectroscopy and theoretical analysis of the equivalent circuit. The charge-transfer and solid-state diffusion resistances proved to be the important factors in the course of high-rate battery discharging of the $\text{LiNi}_{0.5}\text{Mn}_{1.5}\text{O}_4$ spinel materials. Especially in the case of the ordered structure, it was demonstrated that the charge-transfer resistance has the most severe effect on the total dc polarization. Moreover, in order to increase the electrochemically active surface area and reduce the diffusion lengths, the one-dimensional nano-structured electrode was prepared via sol-gel based template synthesis. The nano-structured electrodes prepared in this study significantly improved the rate performance of the $\text{LiNi}_{0.5}\text{Mn}_{1.5}\text{O}_4$ spinel materials with the reduced charge-transfer and diffusion resistances, even though the resistances from the multilayer surface films were deteriorated.

Acknowledgments

Acknowledgment is made to the donors of the American Chemical Society Petroleum Research Fund (51311-DNI10) for support of this research. The authors acknowledge the use of the UCSD Nano3 Facility supported by the Calit2 and the Cryo-Electron Microscopy Facility supported by NIH grants to Dr. Timothy S. Baker and a gift from the Agouron Institute to UCSD.

References

1. R. F. Service, *Science*, **332**, 1494 (2011).
2. P. Yang and J.-M. Tarascon, *Nat. Mater.*, **11**, 560 (2012).
3. K. Ariyoshi, Y. Makimura, and T. Ohzuku, in *Lithium Ion Rechargeable Batteries*, p. 11, Wiley-VCH Verlag GmbH & Co. KGaA (2010).
4. J. Xiao, X. Chen, P. V. Sushko, M. L. Sushko, L. Kovarik, J. Feng, Z. Deng, J. Zheng, G. L. Graff, Z. Nie, D. Choi, J. Liu, J.-G. Zhang, and M. S. Whittingham, *Adv. Mater.*, **24**, 2109 (2012).
5. M.-C. Yang, B. Xu, J.-H. Cheng, C.-J. Pan, B.-J. Hwang, and Y. S. Meng, *Chem. Mat.*, **23**, 2832 (2011).
6. B. Xu, D. Qian, Z. Wang, and Y. S. Meng, *Materials Science and Engineering: R: Reports*, **73**, 51 (2012).
7. J. Cabana, M. Casas-Cabanas, F. O. Omenya, N. A. Chernova, D. Zeng, M. S. Whittingham, and C. P. Grey, *Chem. Mat.*, **24**, 2952 (2012).
8. J. Song, D. W. Shin, Y. Lu, C. D. Amos, A. Manthiram, and J. B. Goodenough, *Chem. Mat.*, **24**, 3101 (2012).
9. L. Wang, H. Li, X. Huang, and E. Baudrin, *Solid State Ion.*, **193**, 32 (2011).
10. H. M. Cho, Y. J. Park, and H. C. Shin, *J. Electrochem. Soc.*, **157**, A8 (2010).

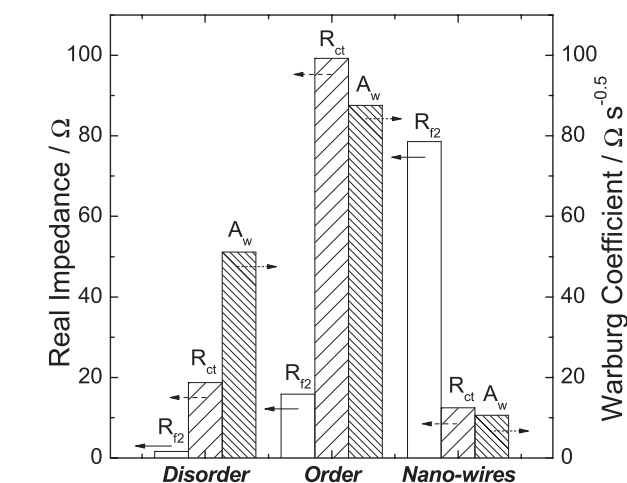


Figure 9. Changes in individual real impedances and Warburg coefficient with the disordered and ordered structure, and its nano-structured electrode.

11. H. M. Cho and H. C. Shin, in *Lithium batteries research, technology, and applications*, G. R. Dahlin and K. E. Strom Editors, p. 73, Nova Science Publishers, New York (2010).
12. H.-M. Cho, W.-S. Choi, J.-Y. Go, S.-E. Bae, and H.-C. Shin, *J. Power Sources*, **198**, 273 (2012).
13. H. M. Cho, Y. J. Park, J. W. Yeon, and H. C. Shin, *Electron. Mater. Lett.*, **5**, 169 (2009).
14. K. J. Carroll, M.-C. Yang, G. M. Veith, N. J. Dudney, and Y. S. Meng, *Electrochemical and Solid-State Letters*, **15**, A72 (2012).
15. C. J. Patrissi and C. R. Martin, *J. Electrochem. Soc.*, **146**, 3176 (1999).
16. C. R. Sides, F. Croce, V. Y. Young, C. R. Martin, and B. Scrosati, *Electrochemical and Solid-State Letters*, **8**, A484 (2005).
17. C. R. Sides and C. R. Martin, in *Modern Aspects of Electrochemistry No. 40*, R. E. White, C. G. Vayenas, and M. E. Gamboa-Aldeco Editors, p. 75, Springer, New York (2007).
18. N. Amdouni, K. Zaghib, F. Gendron, A. Mauger, and C. Julien, *Ionics*, **12**, 117 (2006).
19. J. H. Kim, S. T. Myung, C. S. Yoon, S. G. Kang, and Y. K. Sun, *Chem. Mat.*, **16**, 906 (2004).
20. K. M. Shaju and P. G. Bruce, *Dalton Transactions*, **40**, 5471 (2008).
21. R. D. Shannon, *Acta Crystallographica Section A*, **32**, 751 (1976).
22. S.-I. Pyun and J.-S. Bae, *Electrochim. Acta*, **41**, 919 (1996).
23. M. D. Levi and D. Aurbach, *The Journal of Physical Chemistry B*, **101**, 4630 (1997).
24. M. D. Levi, G. Salitra, B. Markovsky, H. Teller, D. Aurbach, U. Heider, and L. Heider, *J. Electrochem. Soc.*, **146**, 1279 (1999).
25. E. Barsoukov and J. R. Macdonald, *Impedance spectroscopy : theory, experiment, and applications*, p. xvii, Wiley-Interscience, Hoboken, N.J. (2005).
26. D. Aurbach, *J. Power Sources*, **89**, 206 (2000).
27. D. Aurbach, in *Advances in Lithium-Ion Batteries*, W. Schalkwijk and B. Scrosati Editors, p. 7, Springer US (2002).
28. D. Aurbach, M. D. Levi, K. Gamulski, B. Markovsky, G. Salitra, E. Levi, U. Heider, L. Heider, and R. Oesten, *J. Power Sources*, **81-82**, 472 (1999).
29. D. Aurbach, M. D. Levi, E. Levi, H. Teller, B. Markovsky, G. Salitra, U. Heider, and L. Heider, *J. Electrochem. Soc.*, **145**, 3024 (1998).
30. H.-C. Shin and M. Liu, in *Progress in Corrosion Science and Engineering II*, S.-I. Pyun and J.-W. Lee Editors, p. 297, Springer, New York (2012).
31. P. G. Bruce, B. Scrosati, and J.-M. Tarascon, *Angewandte Chemie International Edition*, **47**, 2930 (2008).
32. R. Pitchai, V. Thavasi, S. G. Mhaisalkar, and S. Ramakrishna, *J. Mater. Chem.*, **21**, 11040 (2011).
33. K. T. Lee and J. Cho, *Nano Today*, **6**, 28 (2011).
34. J. B. Goodenough and Y. Kim, *Chem. Mat.*, **22**, 587 (2010).
35. J. Cabana, H. H. Zheng, A. K. Shukla, C. Kim, V. S. Battaglia, and M. Kunduraci, *J. Electrochem. Soc.*, **158**, A997 (2011).
36. N. M. Hagh, F. Cosandey, S. Rangan, R. Bartynski, and G. G. Amatucci, *J. Electrochem. Soc.*, **157**, A305 (2010).
37. G. B. Zhong, Y. Y. Wang, Y. Q. Yu, and C. H. Chen, *J. Power Sources*, **205**, 385 (2012).
38. W. Weppner and R. A. Huggins, *J. Electrochem. Soc.*, **124**, 1569 (1977).
39. E. Markevich, M. D. Levi, and D. Aurbach, *Journal of Electroanalytical Chemistry*, **580**, 231 (2005).